Journal of The Electrochemical Society, 2021 **168** 114510

Modeling Electrokinetics of Oxygen Electrodes in Solid Oxide Electrolyzer Cells

Korey Cook,[1,2] Jacob Wrubel,[2,*] Zhiwen Ma,[2] Kevin Huang,[3,*] and Xinfang Jin[1,*,z]

[1]*Mechanical Engineering Department, University of Massachusetts, Lowell, Massachusetts 01854, United States of America*
[2]*National Renewable Energy Laboratory, Golden, Colorado 80401, United States of America*
[3]*Mechanical Engineering Department, University of South Carolina, Columbia, South Carolina 29201, United States of America*

A microscale model is presented in this study to simulate electrode kinetics of the oxygen electrode in a solid oxide electrolyzer cell (SOEC). Two mixed ionic/electronic conducting structures are examined for the oxygen producing electrode in this work: single layer porous lanthanum strontium cobalt ferrite (LSCF), and bilayer LSCF/SCT (strontium cobalt tantalum oxide) structures. A yttrium-stabilized zirconia (YSZ) electrolyte separates the hydrogen and oxygen electrodes, as well as a gadolinium doped-ceria (GDC) buffer layer on the oxygen electrode side. Electrochemical reactions occurring at the two-phase boundaries (2PBs) and three-phase boundaries (3PBs) of single-layer LSCF and bilayer LSCF/SCT oxygen electrodes are modeled under various SOEC voltages with lattice oxygen stoichiometry as the key output. The results reveal that there exists a competition in electrode kinetics between 2PBs and 3PBs, but 3PBs are the primary reactive sites for single-layer LSCF oxygen electrode under high voltages. These locations experience the greatest oxygen stoichiometry variations and are therefore the most likely locations for dimensional changes. By applying an active SCT layer over LSCF, the 2PBs become activated to compete with the 3PBs, thus alleviating oxygen stoichiometry variations and reducing the likelihood of dimensional change. This strategy could reduce lattice structural expansion, proving to be valuable for electrode-electrolyte delamination prevention and will be the focus of future work.
 [DOI: 10.1149/1945-7111/ac35fc]

Manuscript submitted September 6, 2021; revised manuscript received October 8, 2021. Published November 18, 2021. *This paper is part of the JES Focus Issue on Solid Oxide Fuel Cells (SOFCs) and Electrolysis Cells (SOECs).*

Hydrogen (H_2) is an essential component of our efforts to realize a low-carbon and sustainable energy future. As a fuel/energy carrier with the highest gravimetric energy content (3×higher than gasoline), H_2 can be produced from diverse domestic resources, such as fossil fuels, biomass, and water splitting. It has found use in a variety of domestic industries, such as power generation and manufacturing of steel, cement, ammonia, and other chemicals.[1,2] Currently, more than 95% of bulk H_2 is produced via steam methane reforming (SMR). SMR is a very efficient (>98%) and low-cost ($2/kg H_2) process for making H_2 (also known as Blue H_2), but it emits significant amount of CO_2 (9kg CO_2/kg H_2 produced) into the atmosphere, imposing a negative impact on environment.[3]

Water splitting through electrolysis, thermally driven chemical looping processes including solar thermochemical systems, and light-driven photoelectrochemical processes are attractive alternatives for making clean H_2 (also known as Green H_2). Electrolysis is currently the most studied method for Green H_2.[2] There are three incumbent water electrolyzer technologies differentiated by the electrolytes employed: alkaline solutions, polymer exchange membranes (PEMs) and solid oxides (SOs). While alkaline-based electrolyzers are commercially available, their cost and efficiency of H_2 production are less competitive to SMR (e.g. $5–6/kg-$H_2$ and 60%–70% vs <$2/kg-$H_2$ and >98% for SMR).[3] Low temperature PEM electrolyzers use expensive membranes and noble metal catalysts to produce H_2 at higher cost and slightly higher efficiency (~75%).[4] In contrast, high temperature solid oxide electrolyzers operated at >600 °C[5] are advantageous from a thermodynamic perspective since heat ($T\Delta S$) can be converted into chemical energy (ΔH).[6] This additional heat reduces the overall electrical power (ΔG) requirement, allowing an electrolysis cell to achieve ~100% efficient H_2.[6] Since the thermal energy contribution to the electrolysis reaction can also be obtained from sensible Joule heating produced within the cell, the electrical energy demand is further reduced which decreases the H_2 production price. The bulk of the heat can be provided by an external source such as nuclear power, solar thermal power, or waste heat from a chemical plant.[6] Theoretically, there is no external heat requirement if the electrolyzers operate at the thermoneutral voltage. Due to the above advantages, the research and development on solid oxide-based water electrolyzers have received significant attention.[6–11]

This work focuses on physics-based modeling of high temperature solid oxide electrolysis cells (SOEC). A critical challenge to the development of SOECs is the poor durability at high current (high-H_2 flux) operation associated with the oxygen electrode/electrolyte interface delamination.[9] A clearer fundamental understanding on the delamination mechanisms is critically needed to address this practical problem for SOEC technology commercialization.[11–13] Here in this study, we use a Multiphysics method to simulate oxygen evolution process under electrolysis mode. We specifically consider electrode reactions at two-phase boundaries (2PBs) and three-phase boundaries (3PBs). Electrochemical modeling using each of these boundaries has been previously discussed in literature.[14–19] Specifically, at the solid/gas interface of the mixed ionic and electron conducting (MIEC) oxygen electrodes (OE), there have been debates whether the reaction of interest is chemical or electrochemical in nature.[14,19,20] Adler et al. described this as a purely chemical process governed by the neutral combination of species. However, Huang and Goodenough described this process as an electrochemical reaction.[14,19] Experimental studies have indicated that the gas/MIEC OE interface reaction is a multiple-step process that involves multiple charged species and could be electrochemically driven.[21–23] Inspired by these prior works, we treat the overall reaction as a combination of oxygen evolution (OER, Eq. A·2) and oxygen desorption reactions (ODR, Eq. A·3), shown in Table I. The former is a chemical reaction, whereas the latter is an electrochemical reaction driven by surface overpotential. We hypothesize that competition between the 2PBs and 3PBs results in oxygen stoichiometry variation, which strains the oxygen lattice and is thought to be the source responsible for OE delamination. With the presented microscale electrochemical model, parameters selection, and experimental validation, we show that at high overpotentials the reaction at the 3PB dominates the overall oxygen flux compared to the 2PB. Our model also shows that the 2PB reaction can be appreciably enhanced by adding a thin catalytically active layer of $SrCo_{0.9}Ta_{0.1}O_{3-\delta}$ (SCT),

*Electrochemical Society Member.
[z]E-mail: Xinfang_Jin@uml.edu

Table I. Elementary reactions shown in Fig. 2 expressed using Kröger-Vink notation.[24]

No.	Reaction	Expression
1	$O^x_{O,GDC} + VV^{\cdot\cdot}_{O,LSCF} \rightleftarrows O^x_{O,LSCF} + V^{\cdot\cdot}_{O,GDC}$	$r_1 = i_{01}\left[\frac{c_{V,LSCF}}{c_{V,0,LSCF}}\exp\left(\frac{\alpha_1 F\eta_1}{RT}\right) - \frac{c_{V,GDC}}{c_{V,0,GDC}}\exp\left(-\frac{(1-\alpha_1)F\eta_1}{RT}\right)\right.$
2	$O^X_O + h^{\cdot} + (s) \rightleftarrows O'_s + V^{\cdot\cdot}_O$	$r_2 = k_{des,0}\left[\frac{(1-\theta_o)c_{h,LSCF}}{(1-\theta_{o,0})c_{h,0,LSCF}}\exp\left(\frac{\alpha_2 F\Delta\chi_h}{RT}\right) - \frac{\theta_o c_{V,LSCF}}{\theta_{o,0}c_{V,0,LSCF}}\exp\left(-\frac{(1-\alpha_2)F\Delta\chi_h}{RT}\right)\right.$
3	$O'_s + h^{\cdot} \rightleftarrows \frac{1}{2}O_{2(g)} + (s)$	$r_3 = k_f{\theta_o}^2 - k_b P_{O2}{\theta_s}^2$
4	$O^x_{O,GDC} + 2h^{\cdot}_{LSCF} \rightleftarrows V^{\cdot\cdot}_{O,GDC} + \frac{1}{2}O_{2(g)}$	$r_4 = i_{04}\left[\frac{c_{h,LSCF}}{c_{h,0,LSCF}}\exp\left(\frac{\alpha_4 F\eta_4}{RT}\right) - \frac{c_{V,GDC}}{c_{V,0,GDC}}\exp\left(-\frac{(1-\alpha_4)F\eta_4}{RT}\right)\right]$

which reduces the variations of lattice oxygen stoichiometry and offers a solution to mitigate OE delamination.

Microscale Model Theory

To investigate how the cell current (oxygen flux) affects lattice oxygen stoichiometry and ultimately the OE delamination mechanisms, a numerical microscale model was developed. The numerical model was built in COMSOL 5.4 using the coefficient form partial differential equation (PDE) module. The primary governing equations, and boundary conditions for each domain are shown in Tables I and II. Figure 1 shows the geometry and domain of interest. Oxygen ions are transported sequentially from the hydrogen electrode (HE) (bottom to top) through an electrolyte of 8 mol. % Y_2O_3-doped ZrO_2, (YSZ), a buffer layer of 10 mol. % Gd_2O_3-doped CeO_2 (GDC), and finally through a mostly electronically conductive OE of $La_{0.6}Sr_{0.4}Fe_{0.6}Co_{0.4}O_{3-\delta}$ (LSCF). Gas/solid interface reactions occur at the surface of both GDC and LSCF where lattice oxygen O^X_O becomes oxygen gas. Electrons move from the LSCF to an external circuit. A cylindrical geometry was chosen to represent the porous OE with LSCF columns stacking side-by-side to form the solid matrix.[12] This homogenization approach is an idealization of the layers of the OE, with the actual microstructure having a much more complex morphology. However, the geometry of the present work allows us to gain fundamental insight into the highly coupled reactive transport processes without being complicated by microstructural effects. We acknowledge that a complete 3D porous microstructure could be obtained using a method such as synchrotron-based 3D imaging to represent the domain more accurately, which will be undertaken in future work.[12]

The transport pathways involve several charged species, including electrons (e'), electron holes ($h^{\cdot}$), and oxygen vacancies ($V^{\cdot\cdot}$) expressed using Kröger-Vink notation.[24] Lattice defects arise either from doping or from reduction/oxidation reactions at solid/gas interface. Several types of boundaries exist within the model. Treatment of each of these boundaries and other detailed considerations are discussed below. The structure of the mixed-conducting LSCF sub-phase is represented by an array of identical cylindrical rods, as shown in Fig. 1. Since the OE material is highly electrically conductive and continuous, it can be viewed as an iso-potential conductor with a uniform electrochemical potential of electrons.[12]

Three types of interfaces are considered in the present model: 2PBs dominated by continuous charge transport across solid layers (YSZ/GDC and GDC/LSCF); 2PBs present at the interface of the electrode and $O_{2\,(g)}$ ($O_{2\,(g)}$/LSCF and $O_{2(g)}$/GDC); and 3PBs present at the interface of the electrode/$O_{2\,(g)}$/electrolyte layers ($O_{2\,(g)}$/LSCF/GDC). Implementation of each of these boundaries has been discussed in the literature.[14–19] The dimensions of each domain are listed in Table III.

There are two major transport pathways that oxygen vacancies follow through the SOEC's microstructure to the electrode's surface where oxygen gas is produced through OER and ODR. The proposed mathematical description of these pathways and the governing equations for each reaction are listed in Table II. In the 2PB pathway, lattice oxygen in LSCF and GDC will exchange ionic current at their interface ①, then the lattice oxygen in LSCF becomes an oxygen atom on the surface with an electron and an oxygen vacancy ②, and lastly, it is deadsorbed from the surface and becomes a free oxygen molecule in the gas phase ③. The first two reactions are electrochemical in nature, governed by the Butler-Volmer like expression; the last reaction is purely chemical and is dependent on the LSCF surface oxygen site coverage and the oxygen partial pressure in the gas phase. In the triple-phase boundary (3PB) pathway, only one electrochemical reaction occurs ④, which involves three phases: gas (oxygen), solid LSCF (electron), and solid GDC (vacancy). So, reaction ④ is occurring in parallel with reactions ①, ②, and ③.

The double layer at the gas/electrode interface has been previously modeled based on the Helmholtz double layer theory.[25,26] A representation of this is shown in Fig. 2. Details of the surface overpotential estimation can be found in Appendix A. LSCF is an electronically conductive MIEC OE and it's assumed that the Fermi level (electrochemical potential of electrons) is uniform across its entire thickness. Therefore, the charge transport model within this domain can simply be reduced to the modified Fick's first law.[8] Nernst-Planck theory is still needed to describe transport across the GDC electrolyte as it does not have a uniform Fermi level potential, with a relatively low electronic conductivity but a very high ionic conductivity. Details of the governing equations and boundary conditions are provided in Table II.

Experimental Validation and Model Parameters

The principal defects and their formation reactions in the materials of interest, including YSZ, GDC and LSCF, are listed in Table B·I of Appendix B. The concentration of the charged species will affect the properties of the materials, such as conductivity. In this work, all the transport or concentration parameters used in the modeling are from experimental measurements published in the open literature; they are listed in Table B·II of Appendix B. The mobility, concentration, diffusivity, and conductivity are related

Table II. Governing equations and boundary conditions.

Domain	Governing Equations	Charge Carriers	Dependent Variables	Boundary Conditions	
YSZ	$\nabla \cdot J_{V,YSZ} = 0$	V	$\varnothing$	YSZ/Ni-GDC (2PB)	$J_{V,YSZ} = \frac{i_o}{F\ z_V}[e^{\left(\frac{\alpha_n F\ \eta_{s,YGN}}{RT}\right)} - e^{\left(\frac{-\alpha_p F\ \eta_{s,YGN}}{RT}\right)}]$
	$J_{V,YSZ} = \frac{\sigma_k \nabla \phi}{F z_V}$				
				YSZ/GDC (2PB)	$\phi_{eq} = 0$
					$J_{V,YSZ} = J_{V,GDC},\ \phi_{YSZ} = \phi_{GDC}$
GDC	$\nabla \cdot J_{V,GDC} = 0$	$V,\ e$	$c_v,\ \varnothing$	YSZ/GDC (2PB)	$J_{V,YSZ} = J_{V,GDC},\ \phi_{YSZ} = \phi_{GDC},\ J_{e,gdc} = 0$
	$J_{V,GDC} = -D_{V,GDC}\left(\nabla c_{V,GDC} + \frac{z_V F}{RT} c_{V,GDC} \nabla \phi\right)$				
				GDC/$O_{2(g)}$(2PB)	$J_{V,GDC} = k_{chem,GDC}(c_{V,GDC,o} - c_{V,GDC}),$
					$J_{e,GDC} = 2k_{chem,GDC}(c_{V,GDC,o} - c_{V,GDC})$
	$\nabla \cdot J_{e,GDC} = 0$			GDC/LSCF/$O_{2(g)}$ (3PB)	$J_{V,G3PB} = \frac{i_o}{2F}[e^{\left(\frac{\alpha_n F\ \eta_{s,G3PB}}{RT}\right)} - e^{\left(\frac{-\alpha_p F\ \eta_{s,G3PB}}{RT}\right)}]$
	$J_{e,GDC} = -D_{e,GDC}\left(\nabla c_{e,GDC} + \frac{z_e F}{RT} c_{e,GDC} \nabla \phi\right)$				
				GDC/LSCF(2PB)	$\eta_{s,G3PB} = V_{cell} - \phi_{GDC} - E_{eq},\ J_{e,GDC} = 0$
					$J_{V,GL} = \frac{i_0}{F\ z_V}[e^{\left(\frac{\alpha_n F\ \eta_{s,GLV}}{RT}\right)} - e^{\left(\frac{-\alpha_p F\ \eta_{s,GLV}}{RT}\right)}]$
					$\eta_{s,GLV} = \frac{\mu_{V,LSCF} - \mu_{V,GDC}}{2F} - E_{eq}$
					$J_{e,GL} = \frac{i_0}{F\ z_e}[e^{\left(\frac{\alpha_n F\ \eta_{s,GLe}}{RT}\right)} - e^{\left(\frac{-\alpha_p F\ \eta_{s,GLe}}{RT}\right)}]$
					$\eta_{s,GLe} = \frac{\mu_{h,LSCF} + \mu_{e,GDC}}{F} - E_{eq}$
LSCF	$\nabla \cdot J_{V,LSCF} = 0$	V	c_V	LSCF/$O_{2(g)}$(2PB)	$J_{V,LSCF} = k_{chem,LSCF}(c_{V,LSCF,o} - c_{V,LSCF})$
	$J_{V,LSCF} = -D_{V,LSCF}(\nabla c_{V,LSCF})$		LSCF/GDC (2PB)		$J_{V,LSCF} = J_{V,GL}$

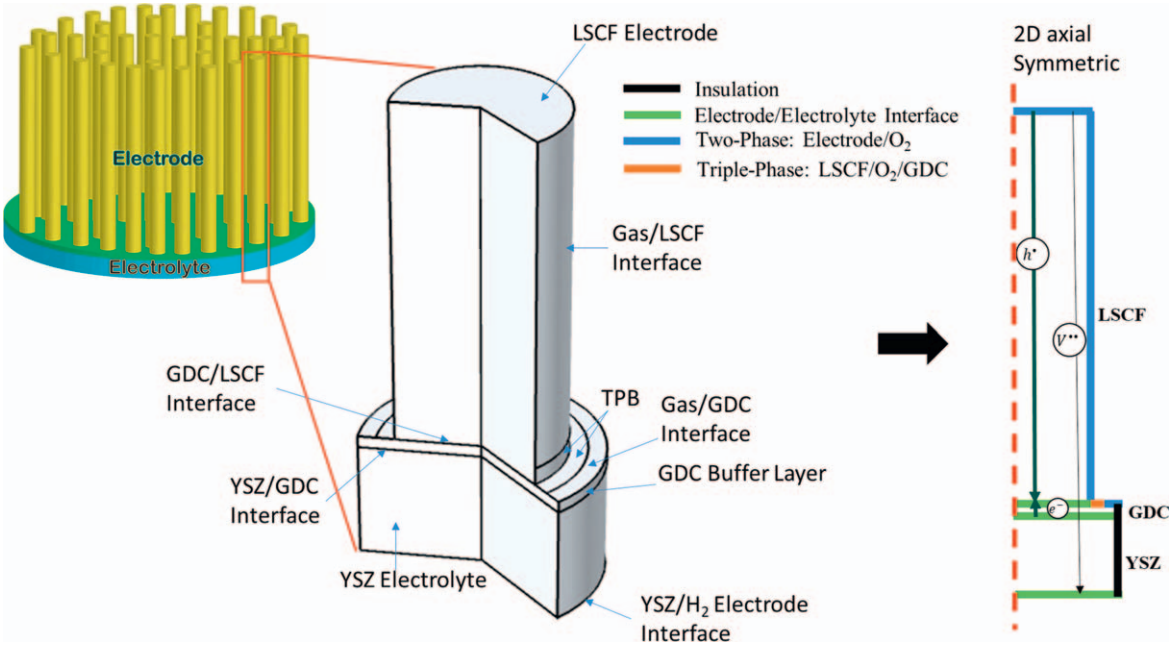

Figure 1. Diagram of columnar OE structure and model domain.[12]

Table III. Dimensions of the computational domain.

Material/Domain	Radius	Length
YSZ Electrolyte	10 μm	10 μm
GDC Buffer Layer	10 μm	1 μm
LSCF Electrode	7 μm	30 μm
3PB	—	1.5 μm
2PB	—	30 μm

through the Nernst Einstein equation in the table. The electron hole mobility in LSCF is assumed to be the same as that of electrons in GDC.

There are two OE designs to be simulated: single layer (with LSCF) and bilayer (with LSCF/SCT bilayer), as shown in Fig. 3a. The thickness of the SCT layer is on the order of a few nanometers, and its dimension is almost negligible compared to the bulk LSCF layer in tens of microns; therefore, we assume that SCT will only affect the surface oxygen exchange kinetics and will not change the bulk transport of oxygen vacancy and holes in the LSCF phase. With OE overpotential vs current density data obtained from University of South Carolina, the electrochemical parameters were obtained by fitting the experimental data and are shown in Fig. 3b; the obtained fitting parameters are listed in Table IV.

According to Mebane et al. and Kilner et al., the reactions at the air-exposed surface in MIECs are rate limited by oxygen evolution for SOEC mode and oxygen incorporation for SOFC mode.[30,31] Therefore, oxygen desorption can be considered fast and in equilibrium.[29,31] The rate constant of OER and equilibrium surface oxygen coverage obtained by this study is on a similar order of magnitude reported by Gong et al., but several orders of magnitude higher than that reported by Mebane et al. for oxygen incorporation reaction.[15,29] Therefore, we think a direct comparison is not meaningful. It is important to mention that our microscale model did not consider the effect of microstructural properties of the electrode, such as tortuosity and specific surface area. Similar limitations are

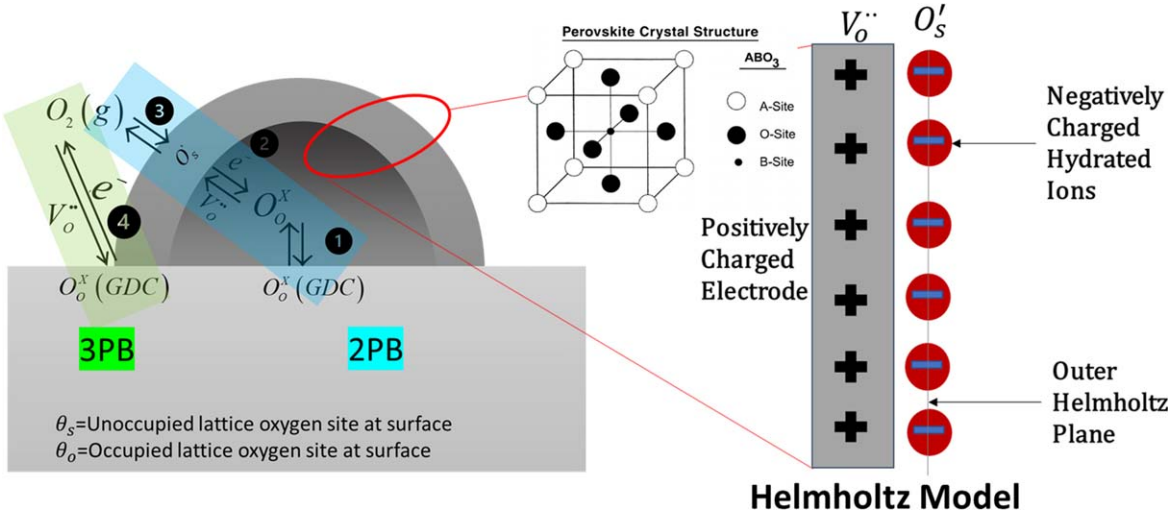

Figure 2. Diagram of transport pathways/reactions and diagram of Helmholtz Model used to demonstrate the separation of charge at an electrode-electrolyte interface.[25,26]

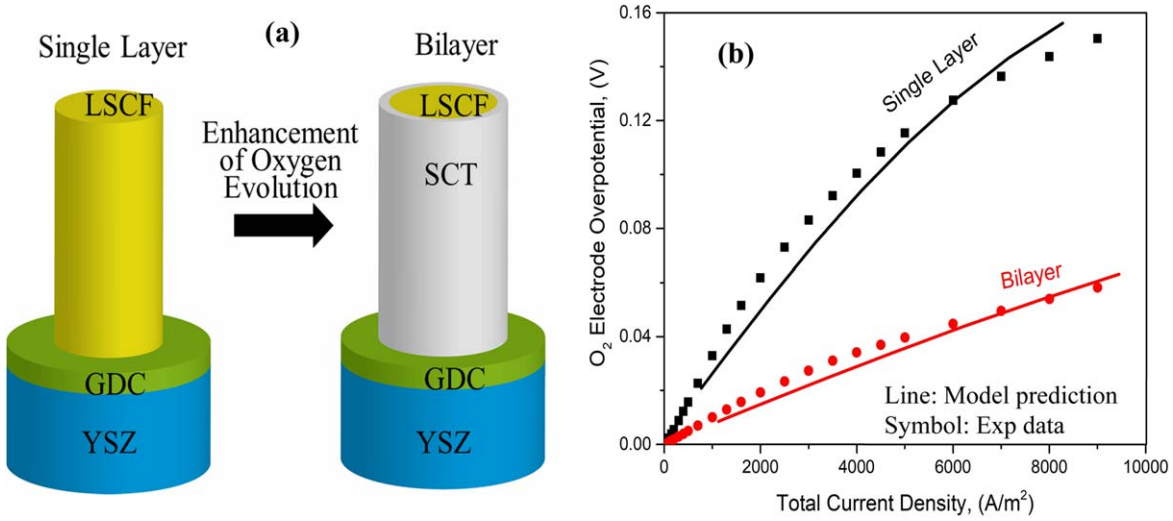

Figure 3. Comparison of oxygen electrode overpotential as a function of current density in both the single and bilayer configurations.

Table IV. Reaction kinetic parameters.

Interface	Parameters	Unit	Single Layer	Bilayer	References
YSZ/HE (2PB)	Exchange current density	A m^{-2}	4000	4000	27
GDC/LSCF (2PB)	Exchange current density[a)]	A m^{-2}	3600	11000	27
Gas/GDC/LSCF (3PB)	Exchange current density[a)]	A m^{-2}	7200	22000	27
Gas/LSCF (2PB)	Equilibrium surface oxygen coverage	1	0.068	0.068	15, 28
Gas/GDC (2PB)	Reaction rate constant	mol m^{-2}/s	0.019	0.019	15, 29
Gas/LSCF (2PB)	Reaction rate constant backward oxygen desorption[a)]	mol m^{-2}/s	0.72	2.2	15, 27, 29
	Reaction rate constant forward oxygen desorption[a)]	mol m^{-2}/s	28.8	88	15, 27, 29
	Reaction rate constant for oxygen evolution[a)]	mol m^{-2} s^{-1}	0.01206	0.03685	15, 27, 29
	Surface overpotential	V	1.07θ	1.07θ	30

a) indicates that the parameter is adjusted to fit the model with experimental data.

also true for the exchange current density values. Therefore, the results of our modeling are more meaningful for relative comparison of single layer vsbilayer OE designs.

Results

With the experimentally validated electrochemical parameters, electrochemical behaviors of single-layer LSCF and bilayer LSCF/SCT OEs are simulated by encompassing OER/ODR at both 2PBs and 3PBs pathways. The competition between the two pathways is represented by the ratio of individual current passing each pathway as a function of cell voltage, while surface oxygen site coverage is also calculated. More importantly, variations in oxygen-vacancy concentration as well as overall lattice oxygen stoichiometry at 2PBs and 3PBs are computed to illustrate the critical role of oxygen stoichiometry in OE delamination.

Competition between transport pathways.—Figures 4 and 5 show the results of parametric studies at various voltages. Analyses were performed while varying the rate of the ODR and OER by 0.1 to 10 folds. The ratio of current through each type of boundary was studied for both the single and bilayer OE configurations. As shown in Fig. 4, the resulting current ratio in the single layer configuration demonstrates that the reactions at the 3PB dominates the 2PBs reaction when operating at high voltages. At lower voltage, such as 1.2 V, 2PBs contribute to a higher percentage of the overall current. Varying the reaction rate constants (k_{des} and k_{evo}) has different effects on the current ratio. As shown in Fig. 4a, the ODR does not influence the current ratio appreciably, but the effect brought by the OER is greater. Figure 4b shows that the enhanced which was 10 times the equilibrium value, could potentially extend 2PBs transport pathway to dominate the overall current in the whole operating range.

A second layer of SCT in a few nanometers was added in both the numerical model and experiments to enhance the overall rate of oxygen evolution. This layer is highly electronically conductive and catalytically active which decreases the overpotential necessary to overcome activation barriers. Since its thickness is on the scale of nanometer, which is much smaller compared to the size of the LSCF backbone, the SCT layer is assumed to only modify the surface oxygen exchange kinetics and the bulk transport properties of LSCF stay unchanged. Figure 5 shows the modeling results of the bilayer OE. In the whole operating range, 2PBs transport is at a higher ratio of current compared to its counterpart at 3PBs. This indicates that with an added layer of SCT, the gas/OE interface reaction has been significantly enhanced. Figures 5a and 5b show similar results when the reaction rate is modified, *i.e.,* the ODR's current ratio is not influenced appreciably; whereas the OER rate significantly affects the current ratio and could potentially change the domination of transport pathway.

Surface oxygen site coverage.—The lattice oxygen coverage (θ) at the surface can be estimated using the Helmholtz model, as described in Appendix A.[26] Both the single and bilayer OE configurations, shown in Figs. 6 and 7, had very similar results with increasing potential. For the ODR, a k_{des} that is 10 times smaller than a reference value yields the greatest θ at high potential. For the OER, k_{evo} does not deviate θ value far from equilibrium. Similar trends have been observed for the bilayer design, as shown in Fig. 7.

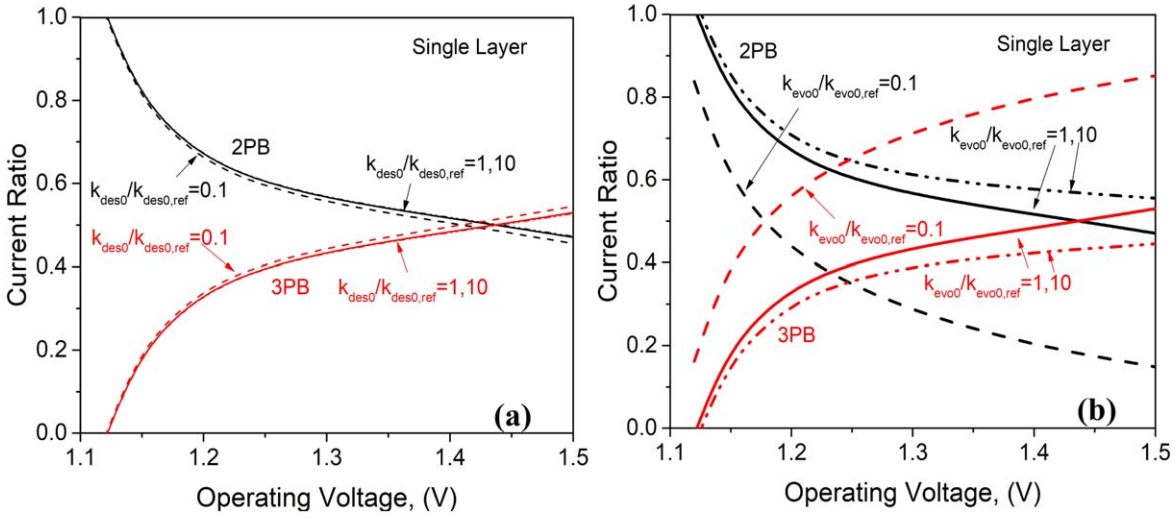

Figure 4. Operating voltage vscurrent ratio with different oxygen desorption (a) and oxygen evolution (b) reaction kinetics for single LSCF layer configuration.

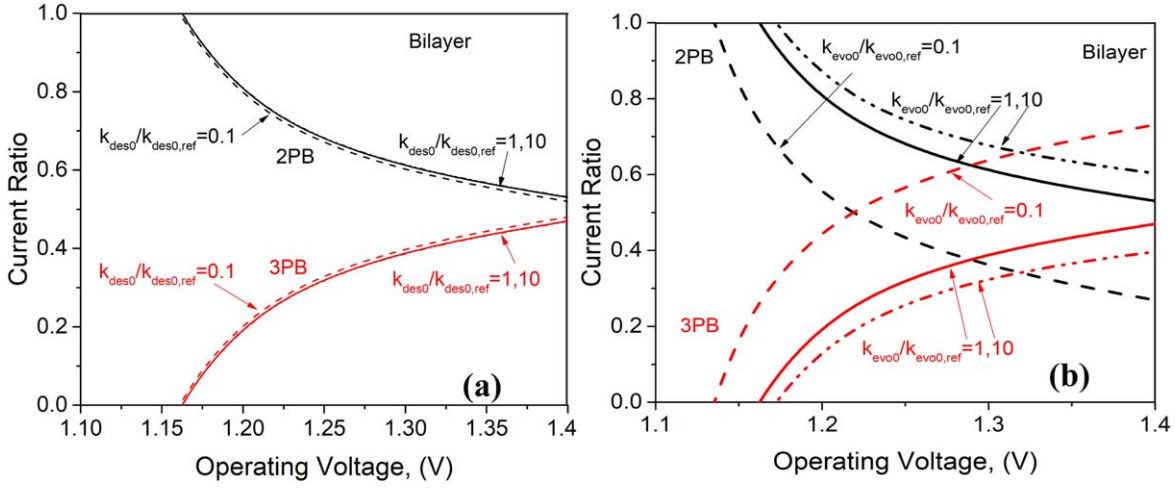

Figure 5. Operating voltage vs current ratio with different oxygen desorption (a) and oxygen evolution (b) reaction kinetics for LSCF/SCT bilayer configuration.

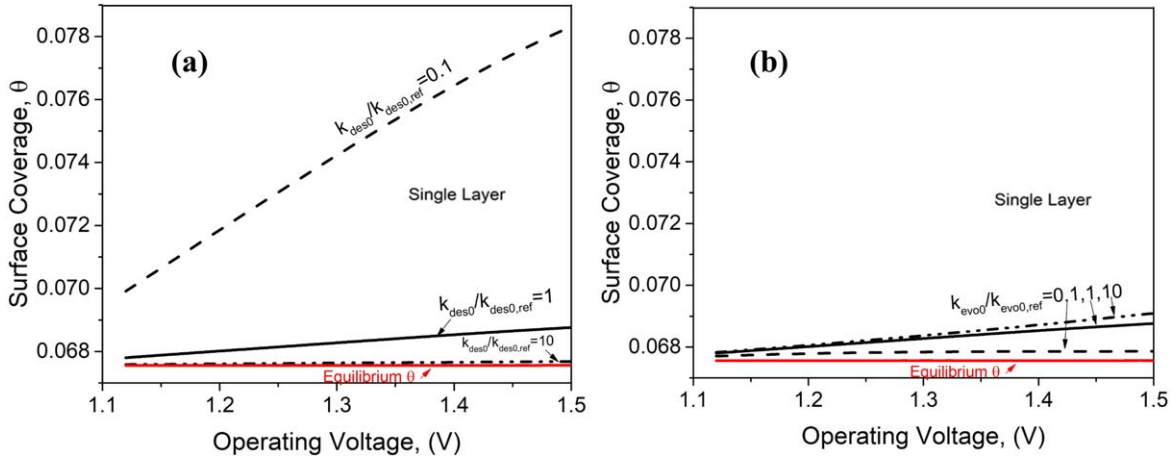

Figure 6. Operating voltage vs surface coverage with different oxygen desorption (a) and oxygen evolution (b) reaction kinetics for single LSCF layer configuration.

Lattice oxygen stoichiometry profile.—Using an axisymmetric modeling method, Fig. 8 shows the lattice oxygen stoichiometry profile of both single-layer and bilayer OEs vs operating voltage. The equilibrium $[O_O^x]$ is taken as 2.966 under 1073 K and 0.21 atm for LSCF.[32] The oxygen stoichiometry evidently deviates less from equilibrium for the bilayer than the single-layer OE. Its gradient varies more significantly along the length direction than the radius direction, which is caused by the higher oxygen ion transport

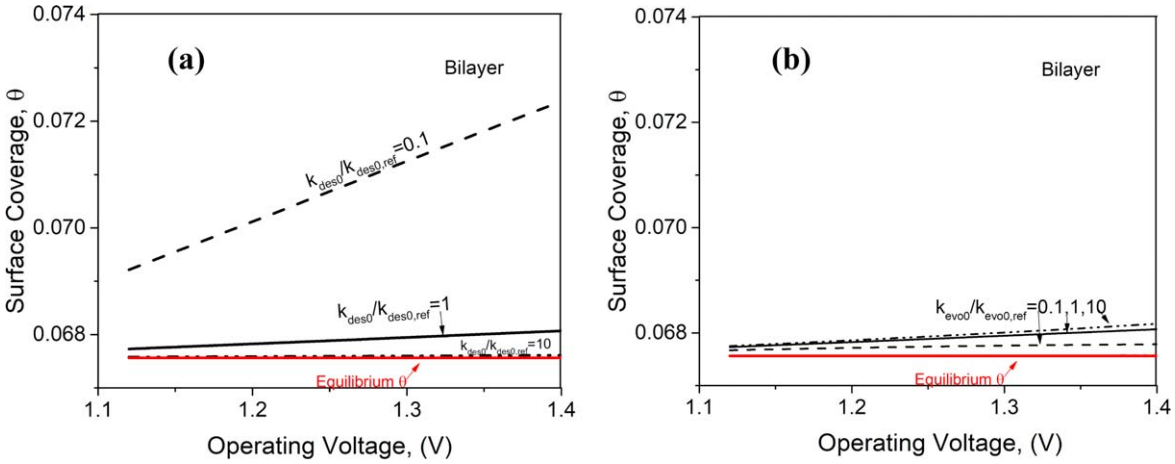

Figure 7. Operating voltage vs surface coverage with different oxygen desorption (a) and oxygen evolution (b) reaction kinetics for LSCF/SCT bilayer configuration.

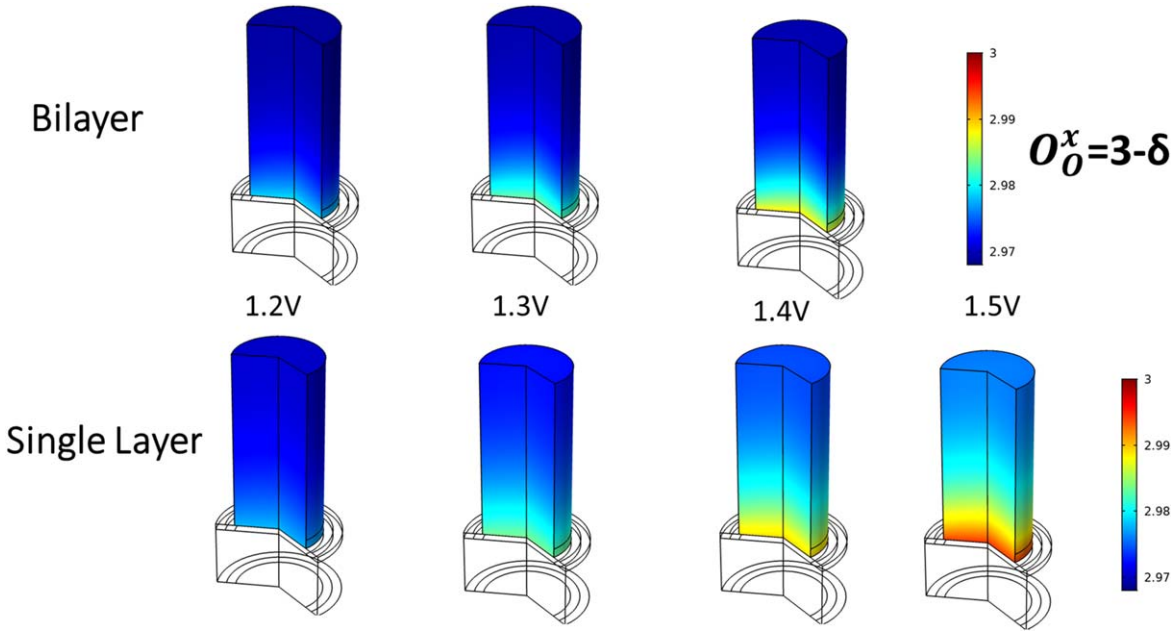

Figure 8. Lattice oxygen stoichiometry profile as a function voltage for both the single and bilayer configurations.

resistance along the length direction than that in the radius direction. Under the electrolysis mode, with increasing operating voltage, more and more oxygen vacancies are converted into lattice oxygens by the transported oxygen-ions, especially at the interface as indicated by the red color. This elevation of oxygen stoichiometry could cause changes in electrical property and lattice dimensional change of the OE, ultimately affecting the electrocatalytic activity and mechanical bonding between the OE and the electrolyte. Note that we assume the maximum lattice oxygen stoichiometry is 3 to maintain its ABO_3 crystal structure and fulfil the requirements of defect chemistry.

Figures 9 and 10 show the operating voltage vs the lattice oxygen stoichiometry at the gas/OE interface. k_{des} and k_{evo} are varied between 0.1 and 10 folds. The ODR rate has a very limited impact on the lattice oxygen stoichiometry. However, lattice oxygen reaches a plateau as a function of operating voltage with poor k_{evo} reaction kinetics.

Overall electrochemical performance.—To gauge the overall performance of single layer vs bilayer OEs, total current density vs operating voltage is computed and plotted in Figs. 11 and 12. For both OE configurations, current density is hardly affected by the ODR rate k_{des} (Figs. 11a and 12a). The current density under the same voltage is higher for the bilayer OE as expected. The effect of OER rate on the current density is presented in Figs. 11b and 12b. Enhancement of k_{evo} could improve the overall cell performance by raising the current density. For single-layer and bilayer OEs, there are 30% and 20% improvement, respectively, by raising k_{evo} by two orders of magnitude.

Discussion

Comparation among different electrodes.—So far, the results support the original hypothesis that there is competition of electrochemical reactions at the 3PBs and 2PBs. Therefore, a nonuniform lattice oxygen stoichiometry profile occurs in the OE. It can be concluded that OER at gas/OE 2PBs plays a key role in the overall performance. There is a transition from 2PBs to 3PBs transport pathway as operating voltage increases. A correlation between the two pathways is drawn and the relationship can be associated with lattice oxygen stoichiometry variations. The addition of the SCT bilayer proved to enhance the OER rate at the 2PBs and 3PBs. Therefore, we also explored a single layer SCT as the OE and

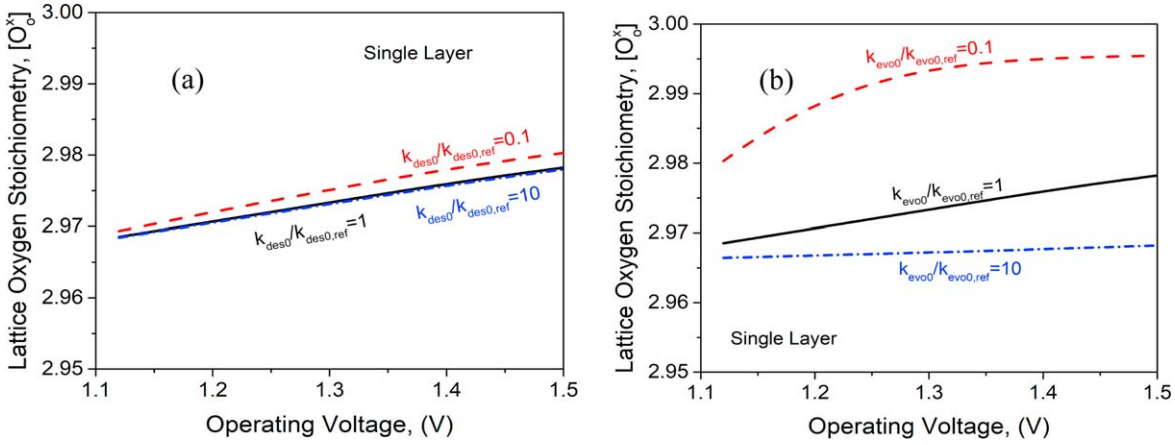

Figure 9. Operating voltage vs lattice oxygen stoichiometry with different oxygen desorption (a) and oxygen evolution (b) reaction kinetics for single LSCF layer configuration.

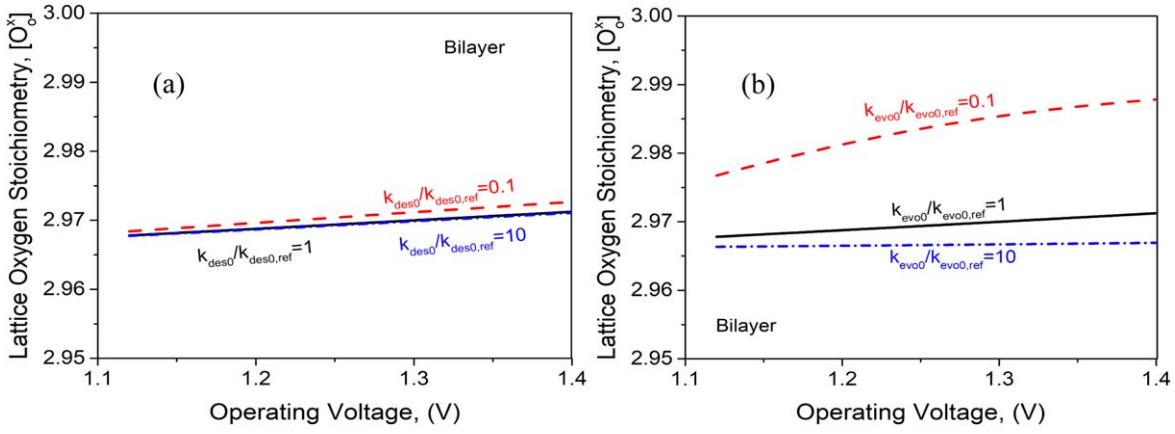

Figure 10. Operating voltage vs lattice oxygen stoichiometry with different oxygen desorption (a) and oxygen evolution (b) reaction kinetics for LSCF/SCT bilayer configuration.

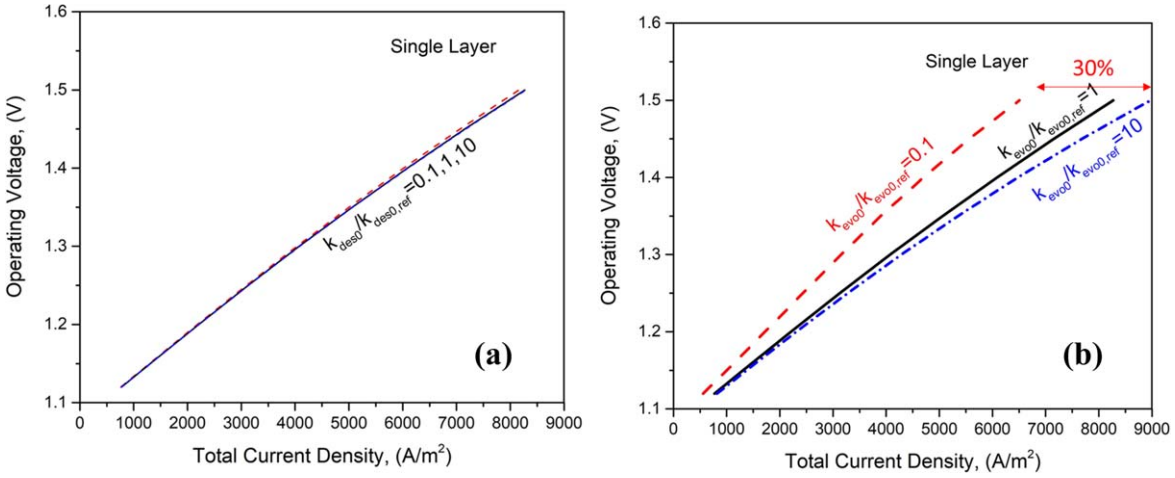

Figure 11. Total current density vs operating voltage with different oxygen desorption (a) oxygen evolution (b) reaction kinetics for singl e LSCF layer configuration.

compared it to the single LSCF layer and LSCF/SCT bilayer configurations.

For SCT single layer design, we assume that (1) surface reaction kinetics is controlled by SCT, so the parameters are the same as that for the bilayer design; (2) charge transport in the bulk is also determined by SCT, the parameters of which are listed in Table B·II in Appendix B according to the open literature. The results among all three scenarios are compared in Fig. 13. In Fig. 13a, it shows that the current from 2PB has a higher percentage in single SCT layer OE compared to the other two OE designs; in Fig. 13b, the lattice

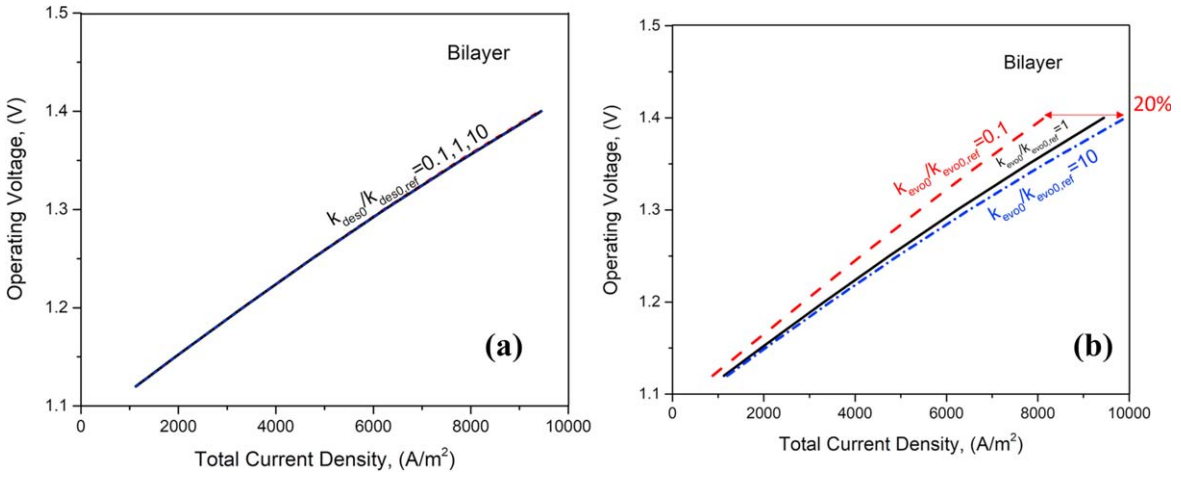

Figure 12. Total current density vs operating voltage with different oxygen desorption (a) oxygen evolution (b) reaction kinetics for LSCF/SCT bilayer configuration.

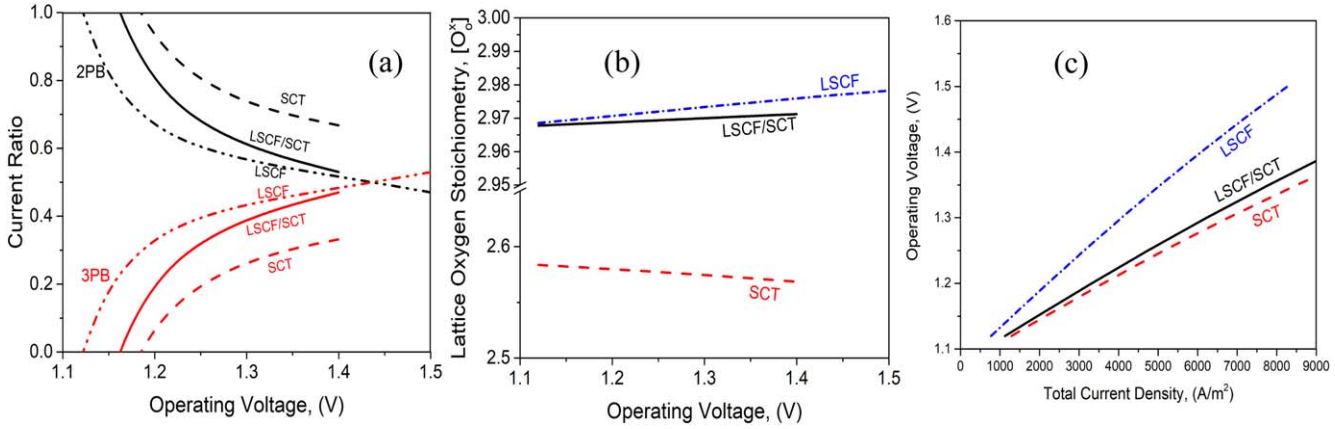

Figure 13. Performance comparison among single SCT layer, LSCF/SCT bilayer, and LSCF single layer configuration: (a) current ratio vs voltage (b) lattice oxygen stoichiometry vs voltage (c) voltage-current curve.

oxygen stoichiometry of SCT layer is much lower than LSCF single layer or LSCF/SCT bilayer, which is resulted from the differences in intrinsic transport properties between SCT and LSCF; in Fig. 13c, a higher current density is observed under the same voltage for SCT single layer. Overall, single SCT layer seems to be the best OE in terms of improving current density and lowering lattice oxygen stoichiometry. However, SCT has a very high thermal expansion coefficient and cannot be used in practical SOECs due to the concerns of manufacturing and thermal cycling operation. The LSCF/SCT bilayer represents a better compromise to overcome the conflict between electrochemical performance and thermal expansion coefficient mismatch.

Figure 14 compares the influence of operating voltage on the current density and lattice oxygen stoichiometry for single-layer LSCF and bilayer LSCF/SCT designs. For the bilayer configuration, under the thermoneutral voltage 1.3 V, the current density is 50% higher than LSCF, whereas lattice oxygen off-stoichiometry is 13% lower than LSCF. Overall, the LSCF/SCT bilayer design offers greater electrochemical performance while simultaneously lowering the risk of lattice dimensional change and thus delamination.

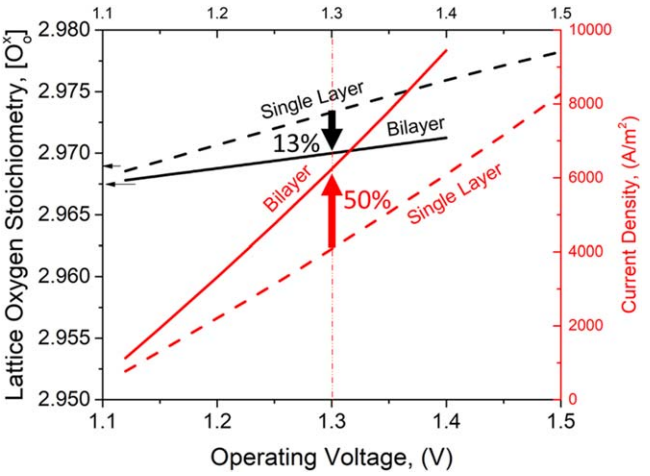

Figure 14. Comparison of lattice oxygen stoichiometry and current density under different operating voltage for single LSCF layer and LSCF/SCT bilayer design.

Limitation of the model.—Although the results from this study are promising, there is still room for improvement. The columnar simplified model might underestimate the microstructural effects on the site ratio of 3PBs and 2PBs. Further studies are needed to expand the current model to practical OEs. This could be done using synchrotron-based 3D imaging technique to generate a detailed 3D domain. OEs are designed to be porous, mixed conducting, multiphase materials capable of transporting gases to and from reaction sites through the pores and oxygen-ion/electrons through the bulk. The resulting microstructure is a tortuous network with spatially varying properties for each individual phase. In many

electrochemical models, this microstructure is homogenized using certain morphological parameters such as porosity, tortuosity, and specific surface area, to represent the electrode as an idealized geometry (e.g., a line, rectangle, disk, rectangular prism, or cylinder). While the homogenized approach is straightforward and can offer improved computational efficiency, it necessarily overlooks some localized, and possibly crucial, transport phenomena. For example, narrow strut-like passages may act like "choke points" and significantly limit transport, effectively shutting down entire regions of the electrode network. These thin sections also concentrate stresses and are likely to experience mechanical failure before thicker sections. Inhibited transport leads to steeper concentration gradients in these regions, thereby leading to increased chemical stresses and further compounding the local stress issue. Similarly, accurate modeling of interfacial delamination relies on the accurate consideration of the interfacial contact area; homogenized shear approaches likely underestimate the interfacial stresses in key areas.

Conclusions

To summarize, we have built a finite element microscale model to investigate the electrochemical transport mechanisms responsible for lattice oxygen stoichiometry variation within a single LSCF and bilayer LSCF/SCT OE operated under electrolyzer mode. The key take-away messages are: (1) there are two primary transport pathways competing for oxygen removal within the OE; (2) the reaction at 3PBs dominates 2PBs under high operating voltage and is likely the cause for lattice oxygen stoichiometry variations and thus OE delamination; (3) adding an active layer of SCT significantly enhances the reaction at 2PBs, thus lowering oxygen stoichiometry gradient and alleviating potential dimensional change/delamination in OE; (4) 3D microstructure measured and reconstructed from X-ray computed tomography should be used to better represent the OE microstructure for high-fidelity modeling.

Acknowledgments

This material is based upon work supported by the U.S. Department of Energy's Office of Energy Efficiency and Renewable Energy (EERE) under the Fuel Cell Technologies Office (FCTO) under Award Number DE-EE-0008842. The authors gratefully acknowledge research support from the HydroGEN Advanced Water Splitting Materials Consortium, established as part of the Energy Materials Network under the U.S. Department of Energy, Office of Energy Efficiency and Renewable Energy, Fuel Cell Technologies Office, under Award Number DE-EE0008091.

Appendix A. Helmholtz Model

In this model, for reaction 2 shown in Table I, the surface overpotential was estimated using Helmholtz model. The lattice constant of LSCF is a = 3.93A. Based on the perovskite ABO_3 crystal structure, there is one oxygen atom per a^2 surface area. Therefore, the oxygen site concentration per area could be calculated by:

$$s = \frac{1}{a^2 N_A} = 7e - 7(\mathrm{mol/m^2}) \quad [A\cdot1]$$

The lattice oxygen coverage θ is defined as:

$$\theta = \frac{O_s'}{sA} \quad [A\cdot2]$$

Where, O_s' is total number of oxygen atoms at the surface, A is the surface area.

Plugging Eq. A·2 into Eq. A·1, we get,

$$O_s' = \theta s A \quad [A\cdot3]$$

There is one negative charge associated with each O_s', the total number of charges at the surface is:

$$Q = F\theta s A \quad [A\cdot4]$$

Where F is the Faraday's constant. Based on the Helmholtz model, the voltage across the two charged plates at a distance d (equals the radius of the O_s' atom) or the surface overpotential χ could be calculated by:

$$\chi = \frac{Qd}{\varepsilon_0 A} = \frac{F\theta s A d}{\varepsilon_0 A} = \frac{Fsd}{\varepsilon_0}\theta \quad [A\cdot5]$$

Assuming $d = 0.14e - 9(m)$, $\varepsilon_0 = 8.854e - 12(C/V/m)$, then,

$$\chi \approx 1.07\cdot\theta(V) \quad [A\cdot6]$$

Based on Eq. A·6, we could see that the surface overpotential is linearly related to the oxygen surface coverage. Since the surface coverage is very small, between 0.01 and 0.1, the surface overpotential is about 0.06V in this model.

Appendix B. Parameters from Experimental Data

Table B·I. Kroger-Vink notation for doping and interface reactions.

Material	Charge carrier	Doping Reaction	Gas/Solid Interface Reaction
YSZ	Y'_{Zr},	$Y_2O_3 = 2Y'_{Zr} + 3O_o^x + V_o^{\cdot\cdot}$	—
GDC	Gd'_{ce}, $V_o^{\cdot\cdot}$, e^-	$Gd_2O_3 = 2Gd'_{ce} + 3O_o^x + V_o^{\cdot\cdot}$	$O_o^x = V_o^{\cdot\cdot} + 2e^- + \frac{1}{2}O_2$
LSCF	Sr'_{La}, $V_o^{\cdot\cdot}$, $Fe_{Fe}^{\cdot}$	$SrO + Fe_{Fe}^x = Sr'_{La} + O_o^x + Fe_{Fe}^{\cdot}$ *Sr*: +2 *La*: +3 *Fe*: +3, +4	$O_o^x + 2Fe_{Fe}^{\cdot} = V_o^{\cdot\cdot} + \frac{1}{2}O_2$

Table B·II. Parameters of material properties.

Material	Properties	Correlation	References
YSZ	Conductivity (S cm^{-1}) vs T (K)	$\log_{10}(\sigma T) = 6.54509 - 5.46453\cdot\frac{1000}{T}$	33
LSCF6446	Oxygen vacancy fraction vs p_{O_2} (atm)	$3-\delta = 2.98941 + 0.03445\cdot \log 10(p_{O_2})$, 1073 K $3-\delta = 3.01635 + 0.03128\cdot \log 10(p_{O_2})$, 973 K $3-\delta = 3.03491 + 0.02717\cdot \log 10(p_{O_2})$, 873 K	32
	Electron hole fraction	$p = [Sr'_{La}] - 2\delta$	—
	Surface Exchange Rate (m s^{-1})	$4.6\cdot10^{-5}$	8
$Ce_{1-x}Gd_xO_{2-\delta}$	Oxygen vacancy fraction vs T(K), p_{O_2} (atm)	$\delta = \frac{9100}{\sqrt{[Gd'_{Ce}]}}\exp\left\{\frac{-220000}{RT}\right\}p_{O_2}^{-1/4} + \frac{[Gd'_{Ce}]}{2}$	34
	Electron fraction	$n = 2\delta - [Gd'_{ce}]$	34
	Oxygen vacancy mobility (cm^2/*V*/*s*) vs T(K)	$\log_{10}(\mu_{i,10}T) = 2.4656 - 3.40416\cdot\frac{1000}{T}$ $\log_{10}(\mu_{i,20}T) = 2.36515 - 3.56931\cdot\frac{1000}{T}$	35
	Electron mobility (cm^2/*V*/*s*) vs T(K)	$\log_{10}(\mu_{e,10}T) = 4.1943 - 4.30072\cdot\frac{1000}{T}$ $\log_{10}(\mu_{e,20}T) = 2.63204 - 2.6264\cdot\frac{1000}{T}$	35
	Diffusivity (cm^2 s^{-1})	$D_i = \frac{\mu_i RT}{F}$	—
	Conductivity (S cm^{-1})	$\sigma_i = \frac{{Z_i}^2F^2D_iC_i}{RT} = {Z_i}^2F\mu_iC_i$	—
	Fraction to molar volume concentration (mol m^{-3})	$c_i = \frac{\delta}{V_m}$ $V_m = \frac{a^3\cdot Na}{NA}$, molar volume, (m^3/mol) Na, Avagadro′s number. NA, numberof cationatomsina unit cell.	—
$SrCo_{0.9}Ta_{0.1}O_{3-\delta}$	Oxygen vacancy fraction vs T(K), p_{O_2} (atm)	$\delta_{SCT} = 0.58141 - 0.02155\ln p_{O_2} - 0.14465\frac{1000}{T}$ $-4.20455\times10^{-4}(\ln p_{O_2})^2$ $-0.07021\left(\frac{1000}{T}\right)^2 + 0.00528\frac{1000}{T}\ln p_{O_2}$	36
	Diffusivity (cm^2 s^{-1})	$(4.01\pm0.67)\times\exp\left(-\frac{0.85\pm0.013\ eV}{k_BT}\right)$	
	Surface Exchange Rate (cm s^{-1})	$(0.26\pm0.04)\times\exp\left(-\frac{0.42\pm0.012\ eV}{k_BT}\right)$	

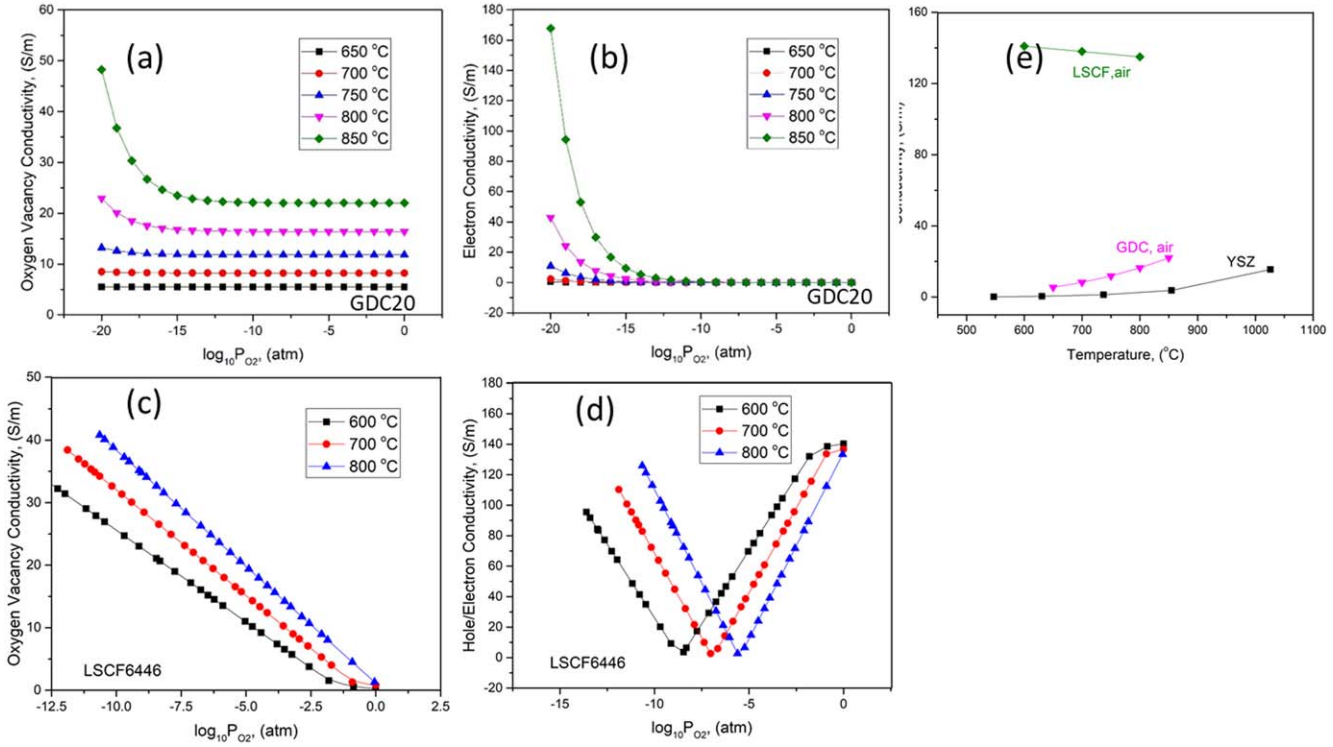

Figure B·1. GDC20 and LSCF6446 conductivity vs PO_2 and Temperature (a) and (c) Oxygen vacancy; (b) and (d) Electron/Hole. (e) Total conductivity comparison among different materials

ORCID

Korey Cook https://orcid.org/0000-0003-1757-1398
Jacob Wrubel https://orcid.org/0000-0002-3347-0768
Kevin Huang https://orcid.org/0000-0002-1232-4593
Xinfang Jin https://orcid.org/0000-0002-3148-4904

References

1. U.S. Department of Energy, "Hydrogen program." (2021), *Energy.gov*, (https://hydrogen.energy.gov/).
2. U.S. Department of Energy-Office of Energy Efficiency & Renewable Energy, "Hydrogen fuel basics." (2021), *Energy.gov*, (https://energy.gov/eere/fuelcells/hydrogen-fuel-basics).
3. U.S. Department of Energy-Golden Field Office, "Thermocatalytic CO_2-Free Production of Hydrogen from hydrocarbon fuels." DE-FC36-99GO10456, 828215 (2004).
4. W. Dönitz and R. Streicher, "Hochtemperatur-elektrolyse von wasserdampf—entwicklungs stand einer neuen technologie zur wasserstoff-erzeugung." *Chem. Ing. Tech.*, **52**, 436 (1980).
5. S. P. Badwal, S. Giddey, and C. Munnings, "Hydrogen production via solid electrolytic routes,." *Wiley Interdisciplinary Reviews: Energy and Environment*, **2**, 473 (2013).
6. M. A. Laguna-Bercero, "Recent advances in high temperature electrolysis using solid oxide fuel cells: a review,." *J. Power Sources*, **203**, 4 (2012).
7. N. Minh, J. Mizusaki, and S. C. Singhal, "Advances in solid oxide fuel cells: review of progress through three decades of the international symposia on solid oxide fuel cells." *ECS Trans.*, **78**, 63 (2017).
8. X. Jin, R. E. White, and K. Huang, "Simulating charge transport in solid oxide mixed ionic and electronic conductors: nernst-planck theory vs modified fick's law." *J. Electrochem. Soc.*, **163**, A2702 (2016).
9. L. Zhang, L. Zhu, and A. V. Virkar, "Modeling of oxygen chemical potential distribution in solid oxide electrolyzer cells." *J. Electrochem. Soc.*, **166**, F1275 (2019).
10. J. P. Stempien, Q. Sun, and S. H. Chan, "'Solid oxide electrolyzer cell modeling: a review." *Journal of Power Technologies*, **93**, 216 (2013).
11. A. V. Virkar, "Mechanism of oxygen electrode delamination in solid oxide electrolyzer cells." *Int. J. Hydrog. Energy*, **35**, 9527 (2010).
12. Y. Lu, C. Kreller, and S. B. Adler, "Measurement and modeling of the impedance characteristics of porous $La_{1-x}Sr_xCoO_{3-\delta}$ electrodes." *J. Electrochem. Soc.*, **156**, B513 (2009).
13. S. N. Rashkeev and M. V. Glazoff, "Atomic-scale mechanisms of oxygen electrode delamination in solid oxide electrolyzer cells." *Int. J. Hydrog. Energy*, **37**, 1280 (2012).
14. S. B. Adler, J. A. Lane, and B. C. H. Steele, "Electrode kinetics of porous mixed-conducting oxygen electrodes." *J. Electrochem. Soc.*, **143**, 3554 (1996).
15. M. Gong, R. S. Gemmen, and X. Liu, "Modeling of oxygen reduction mechanism for 3PB and 2PB pathways at solid oxide fuel cell cathode from multi-step charge transfer." *J. Power Sources*, **201**, 204 (2012).
16. Y. Li, R. Gemmen, and X. Liu, "Oxygen reduction and transportation mechanisms in solid oxide fuel cell cathodes." *J. Power Sources*, **195**, 3345 (2010).
17. S. Liu, J. Suo, and J. Xiao, "'Effects of surface overpotential at the $La_{1-x}Sr_xCo_{1-y}Fe_yO_3$-Yttria stabilized zirconia interface in a model solid oxide fuel cell cathode." *Int. J. Hydrog. Energy*, **33**, 6322 (2008).
18. T. J. Huang and C. L. Chou, "Oxygen dissociation and interfacial transfer rate on performance of SOFCs with metal-added $(LaSr)(CoFe)O_3$-$(Ce,Gd)O_{2-\delta}$ cathodes." *Fuel Cells*, **10**, 718 (2010).
19. K. Huang and J. B. Goodenough, *Solid Oxide Fuel Cell Technology: Principles, Performance and Operations* (Elsevier, Amsterdam) 1 (2009).
20. M. B. Mogensen, E. Ivers-Tiffée, T. Kawada, and S. Adler, "Solid-gas electrochemical interfaces 1." *ECS Meeting*, **231** (2015).
21. F. H. Van Heuveln and H. J. M. Bouwmeester, "Electrode properties of Sr-doped $LaMnO_3$ on Yttria-stabilized zirconia: II. Electrode Kinetics." *J. Electrochem. Soc.*, **144**, 134 (1997).
22. X. J. Chen, K. A. Khor, and S. H. Chan, "Identification of O_2 reduction processes at Yttria stabilized zirconia doped lanthanum manganite interface." *J. Power Sources*, **123**, 17 (2003).
23. J. D. Kim, G. D. Kim, J. W. Moon, Y. I. Park, H. W. Lee, K. Kobayashi, M. Nagai, and C. E. Kim, "Characterization of LSM-YSZ composite electrode by AC impedance spectroscopy." *Solid State Ionics*, **144**, 379 (2001).
24. A. Hammou and S. Georges, "Solid-state electrochemistry: essential course notes and solved exercises." *Springer International Publishing*, **1**, 205 (2020).
25. E. Gongadze, S. Petersen, U. Beck, and U. van Rienen, "Classical models of the interface between an electrode and an electrolyte." *COMSOL Conference*1 (2009).
26. H. Helmholtz, "Studien Über electrische grenzschichten." *Ann. Phy.*, **243**, 337 (1879).
27. X. Jin, *Modeling of Chemical-Mechanical Couplings in Solid Oxide Cells and Reliability Analysis*, University of South Carolina (2014).
28. A. M. Svensson, S. Sunde, and K. Nisşancioğlu, "Mathematical modeling of oxygen exchange and transport in air-perovskite-YSZ interface regions." *J. Electrochem. Soc.*, **144**, 2719 (1997).
29. D. S. Mebane, Y. Liu, and M. Liu, "A two-dimensional model and numerical treatment for mixed conducting thin films: the effect of sheet resistance." *J. Electrochem. Soc.*, **154**, A421 (2007).

30. D. S. Mebane and M. Liu, "Classical, phenomenological analysis of the kinetics of reactions at the gas-exposed surface of mixed ionic electronic conductors." *J. Solid State Electrochem.*, **10**, 575 (2006).
31. J. A. Kilner, R. A. De Souza, and I. C. Fullarton, "Surface exchange of oxygen in mixed conducting perovskite oxides." *Solid State Ion.*, **86–88**, 703 (1996).
32. S. Hashimoto, Y. Fukuda, M. Kuhn, K. Sato, K. Yashiro, and J. Mizusaki, "Oxygen nonstoichiometry and thermo-chemical stability of $La_{0.6}Sr_{0.4}Co_{1-y}Fe_yO_{3-\delta}$ (y=0.2, 0.4, 0.6, 0.8)." *Solid State Ion.*, **181**, 1713 (2010).
33. M. Asadikiya and Y. Zhong, "Oxygen ion mobility and conductivity prediction in cubic yttria-stabilized zirconia single crystals." *J. Mater. Sci.*, **53**, 1699 (2018).
34. A. Atkinson, "Chemically-induced stresses in gadolinium-doped ceria solid oxide fuel cell electrolytes." *Solid State Ion.*, **95**, 249 (1997).
35. S. Wang, T. Kobayashi, M. Dokiya, and T. Hashimoto, "Electrical and ionic conductivity of Gd-doped ceria." *J. Electrochem. Soc.*, **147**, 3606 (2000).
36. T. Yang, X. Jin, and K. Huang, "Transport properties of $SrCo_{0.9}Nb_{0.1}O_{3-\delta}$ and $SrCo_{0.9}Ta_{0.1}O_{3-\delta}$ mixed conductors determined by combined oxygen permeation measurement and phenomenological modeling." *J. Membr. Sci.*, **568**, 47 (2018).